# Interactions between Moisture and Tropical Convection. Part II: The Convective Coupling of Equatorial Waves

BRANDON WOLDING, JULIANA DIAS, AND GEORGE KILADIS

*Physical Sciences Division, NOAA/Earth System Research Laboratory, Boulder, Colorado*

ERIC MALONEY AND MARK BRANSON

*Department of Atmospheric Science, Colorado State University, Fort Collins, Colorado*

## ABSTRACT

The exponential increase in precipitation with increasing column saturation fraction (CSF) is used to investigate the role of moisture in convective coupling. This simple empirical relationship between precipitation and CSF is shown to capture nearly all MJO-related variability in TRMM precipitation, ~80% of equatorial Rossby wave–related variability, and ~75% of east Pacific easterly wave–related variability. In contrast, this empirical relationship only captures roughly half of TRMM precipitation variability associated with Kelvin waves, African easterly waves, and mixed Rossby–gravity waves, suggesting coupling mechanisms other than moisture are playing leading roles in these phenomena. These latter phenomena have strong adiabatically forced vertical motions that could reduce static stability and convective inhibition while simultaneously moistening, creating a more favorable convective environment. Cross-spectra of precipitation and column-integrated dry static energy show enhanced coherence and an out-of-phase relationship in the Kelvin wave, mixed Rossby–gravity wave, and eastward inertio-gravity wave bands, supporting this narrative. The cooperative modulation of precipitation by moisture and temperature anomalies is shown to shorten the convective adjustment time scale (i.e., time scale by which moisture and precipitation are relaxed toward their "background" state) of these phenomena. Speeding the removal of moisture anomalies relative to that of temperature anomalies may allow the latter to assume a more important role in driving moist static energy fluctuations, helping promote the gravity wave character of these phenomena.

## 1. Introduction

The tropics are home to a wide variety of convectively coupled waves: eastward- and westward-propagating disturbances, waves whose structures are symmetric or antisymmetric about the equator, and waves that are predominantly rotational or more divergent. Some waves have "dry" shallow-water analogs (Matsuno 1966), while the analytical analogs of waves thought to be "moisture modes" require the inclusion of moisture as a dynamically active prognostic variable (Sobel et al. 2001; Raymond 2001). Yet other waves have "mixed" characteristics of gravity, Rossby, and/or moisture waves (Adames and Ming 2018; Adames et al. 2019). Convectively coupled equatorial waves (CCEWs) include, but are not limited to, eastward and westward inertio-gravity waves (EIGs and WIGs, respectively), Kelvin waves (KWs), mixed Rossby–gravity waves (MRGs), easterly waves (EWs), equatorial Rossby waves (ERs), and the Madden–Julian oscillation (MJO) (Fuchs et al. 2014; Kiladis et al. 2009; Adames et al. 2019; Zhang 2005; Kiladis et al. 2006; Serra et al. 2008). Collectively CCEWs organize the bulk of tropical rainfall, serve as precursor disturbances for a considerable fraction of tropical cyclones, modulate extratropical weather across a range of time scales, and pose a continuing challenge to global weather and climate models (Avila and Guiney 2000; Thorncroft and Hodges 2001; Matthews et al. 2004; Dias et al. 2018).

While the term CCEW has more traditionally been reserved for phenomena whose basic structures arise as solutions to the shallow-water equations of Matsuno (1966), a more inclusive perspective is adopted here to allow for consideration of phenomena such as the MJO and EWs, whose underlying dynamics remain as an active area of research (Majda and Stechmann 2009;

*Corresponding author*: Brandon Wolding, brandon.wolding@noaa.gov

Sobel and Kim 2012; Roundy 2012b; Wang et al. 2016; Powell 2017; Adames and Ming 2018; Adames et al. 2019). This inclusive perspective is motivated by previous work suggesting CCEWs can be viewed as a spectrum of waves driven by fluctuations in temperature, vorticity, and moisture, whose differing characteristics are determined by the relative magnitudes of the gravity wave, Rossby, and convective adjustment time scales, as well as the effective gross moist stability (GMS) (Sobel et al. 2001; Raymond 2001; Roundy 2012a,b; Sobel and Kim 2012; Adames and Kim 2016; Powell 2017; Adames and Ming 2018; Adames et al. 2019). Effective GMS is a measure of the efficiency with which convection, including its radiative and surface flux feedbacks, imports/exports moist static energy (MSE), thereby supporting (negative effective GMS) or inhibiting (positive effective GMS) moisture–convection feedbacks (Neelin and Held 1987; Raymond et al. 2009; Inoue and Back 2017). Scale analyses performed by these studies suggest that when moisture anomalies persist long enough for gravity waves to damp temperature anomalies and adjust the thermodynamic environment to weak temperature gradient (WTG) balance, MSE fluctuations will be dominated by moisture, and the wave will be more like a moisture mode in character. In contrast, if temperature anomalies are able to persist longer than moisture anomalies, MSE fluctuations will be dominated by temperature, and the wave will be more gravity wave like in character, a point also emphasized by Yasunaga and Mapes (2012). Estimating key scaling parameters using observational and reanalysis data, Adames et al. (2019) suggested that where a given phenomenon falls on the gravity wave to moisture mode spectrum is determined predominantly by its phase speed, with faster waves being more gravity like in character. Following this scaling, the MJO, ERs, EWs, KWs, MRGs, and inertio-gravity waves would comprise a continuum spanning from moisture mode to gravity wave dynamics (Adames et al. 2019).

Despite their differing underlying dynamics, all CCEWs share a common feature: a coupling between large-scale circulations and convection. Conceptually, this coupling can be thought of as a two-way interaction, whereby the large-scale circulations of CCEWs influences convection, which in turn influences the large-scale circulations and energetics of the CCEWs. The large-scale circulations of CCEWs can influence convection through a variety of mechanisms, including modifying the temperature and moisture of the large-scale environment, surface fluxes of heat and moisture, and environmental shear (Mapes 2000; Khouider and Majda 2006; Raymond and Fuchs 2007; Hannah and Maloney 2014; Pritchard and Bretherton 2014; Powell

and Houze 2015; Herman et al. 2016; Moncrieff et al. 2017). Collectively, theoretical, observational, and modeling studies suggest that moisture variations play a crucial role in the convective coupling of phenomena such as the MJO, ERs, and even some EWs, while temperature variations are thought to play a more important role in phenomena of gravity wave character such as inertio-gravity waves and KWs (Mapes 2000; Sobel et al. 2001; Straub and Kiladis 2003; Kuang 2008; Khouider and Majda 2008; Yasunaga and Mapes 2012; Fuchs et al. 2014; Wolding et al. 2016; Adames and Ming 2018; Gonzalez and Jiang 2019). Yet few studies have used a consistent framework to systematically assess convective coupling mechanisms across this broad spectrum of phenomena. Here we provide such an assessment, focusing on the role of moisture in particular.

Tropical precipitation is suppressed in dry environments by the impacts of convective entrainment, and increases roughly exponentially as the environment moistens and column saturation fraction (CSF) increases above some "critical threshold" (Bretherton et al. 2004; Neelin et al. 2009; Ahmed and Schumacher 2017). A companion study, Wolding et al. (2020, hereafter Part I), provides a detailed analysis of this CSF–precipitation relationship, and uses it to identify shortcomings in model representation of moisture–convection coupling. The CSF–precipitation relationship proves to be very useful for examining convective coupling, as it contains valuable information describing how precipitation and convective heating will respond to changes in moisture, as might be caused by the passage of a CCEW. For example, Adames (2017) showed that by linearizing the exponential CSF–precipitation relationship, the magnitude and distribution of MJO precipitation could be diagnosed knowing only the magnitude and distribution of MJO moisture anomalies and the "slowly" varying thermodynamic background in which they occurred.

This study aims to further current understanding of CCEWs by using the CSF–precipitation relationship to

1) assess the degree to which moisture serves as the intermediary through which the large-scale circulations of CCEWs influence convection and
2) show how the different coupling mechanisms of CCEWs can reinforce their own dynamics.

The outline of this paper is as follows. Section 2 details the data and methodologies used in this study. Section 3 examines the role of moisture in the convective coupling of various CCEWs. Further analysis of potential coupling mechanisms, and their implications for wave dynamics, is provided in section 4. Conclusions and discussion are presented in section 5. An assessment of

the geographical variability of the CSF–precipitation relationship is provided in the appendix.

## 2. Data and methodology

Our analysis focuses on oceanic convection, as land surface processes (e.g., strong diurnal surface heating, land–sea-breeze organization) introduce additional complexities to the CSF–precipitation relationship (Ahmed and Schumacher 2015; Bergemann and Jakob 2016; Ahmed and Neelin 2018). In this study we use two observational/reanalysis datasets, Tropical Rainfall Measuring Mission (TRMM) 3B42 precipitation (Huffman et al. 2007), as well as ERA-Interim (hereafter ERAi) (Dee et al. 2011) pressure-level fields of specific humidity $q$, temperature $T$, geopotential height, and horizontal winds. All observational/reanalysis datasets are 6-hourly and have been interpolated to a horizontal grid of $2.5° \times 2.5°$ for the time period of 1998–2015 unless otherwise noted. Saturation specific humidity is calculated from temperature. Mass-weighted vertical integrals, represented by angle brackets $\langle \cdots \rangle$, were performed from 1000 to 100 hPa.

### a. Calculating r-diagnosed precipitation

In this section, the CSF–precipitation relationship is used to create a dataset of "diagnosed" precipitation, whose only source of variability is CSF, which is then compared to TRMM 3B42 precipitation in section 3. As in Bretherton et al. (2004), we use the following empirical relationship to relate CSF and precipitation:

$$P_d(r) = \exp[a_d(r - r_d)], \qquad (1)$$

where

$$r = \frac{\langle q \rangle}{\langle q_s \rangle}, \qquad (2)$$

and $r$ is the CSF, $q$ is specific humidity, $q_s$ is saturation specific humidity, and angle brackets indicate mass-weighted vertical integrals from 1000 to 100 hPa. $a_d$ and $r_d$ are parameters that together describe how steeply and how early the exponential function increases with increasing CSF. In this study, the $a_d$ and $r_d$ parameters are calculated following the methodology of Bretherton et al. (2004). The 6-hourly TRMM 3B42 precipitation and ERAi CSF are first restricted to the geographical location and season of interest. Precipitation rate is separated into bins of CSF of 1% width, and the CSF-binned mean precipitation rate is calculated. The least squares fit of Eq. (1) to the CSF-binned mean precipitation rate is calculated, where bins containing less than 1% of the total observations are excluded from the

fitting. There are several reasons for not extending the curve-fitting analysis into the far tails of the distribution. First, observational/reanalysis products tend to be less reliable near the upper tail of the distribution. Second, the often limited number of observations introduces substantial "noise" to the bin-mean precipitation curve. Third, we seek to understand how small perturbations (~0.1 or less) in CSF around some "background" CSF (typically ~0.65 to 0.75 in the warm pool) impact precipitation, so this is the most relevant part of the CSF–precipitation curve for our study.

Previous studies have found subtle variability in the CSF–precipitation curve over tropical oceans, and have suggested that changing thermodynamic conditions may manifest themselves in variations in the CSF–precipitation curve (Bretherton et al. 2004; Ahmed and Schumacher 2017). We have performed a complimentary analysis of the geographical and seasonal variability of the CSF–precipitation curve, provided in the appendix, which suggests that data should be restricted to the geographical location and season of interest when examining CCEWs in a specific location and/or season. For each CCEW in the subsequent analysis, the geographical location and season used to calculate the CSF–precipitation curve was chosen to correspond to the region and season analyzed in the EOF/basepoint composites, and are given in Tables 1 and 2, respectively. Examples of the CSF-binned mean precipitation rate and corresponding least squares fit for several geographical locations are provided in the appendix.

Once the $a_d$ and $r_d$ parameters have been determined, ERAi CSF can be input to Eq. (1), which will hereafter be referred to as "r-diagnosed precipitation." Note that CSF is the only source of variability in r-diagnosed precipitation, and that, while calculated from 6-hourly data, it also contains variability from longer time scales (Bretherton et al. 2004). To isolate the variability of interest, r-diagnosed precipitation is then bandpass filtered to time scales relevant to the CCEW in question before it is used in compositing. The time scales used for bandpass filtering are given in Tables 1 and 2.

### b. EOF compositing

An EOF basis was chosen as the primary method of compositing because it offers an assessment of the entire life cycle of the CCEW (i.e., transitions through enhanced and suppressed convective phases), in contrast to the basepoint methodology described below, which only offers insight for a few days before/after wave passage. EOF-based indices were developed for each CCEW, largely following methodologies established in existing literature (see, e.g., Kiladis et al. 2016). PC1 and PC2 of each EOF pair were used to create an index,

TABLE 1. Details of the geographical locations and seasons used in the calculation of $r$-diagnosed precipitation for the EOF composites, and the number of days included in the composites. Limits of integration used in the fractional contribution analysis described in section 3b are also provided. MJO, ER, MRG, KW, AEW, and EPEW stand for Madden–Julian oscillation, equatorial Rossby wave, mixed Rossby–gravity wave, Kelvin wave, African easterly wave, and east Pacific easterly wave, respectively.

| | Curve-fitting latitude (°) | Curve-fitting longitude (°) | Curve-fitting season | $a$ parameter | Bandpass-filtering high-frequency time scale (days) | Bandpass-filtering low-frequency time scale (days) | Min, max days in composite | Fractional contribution integration limits time | Fractional contribution integration limits latitude (°) | Fractional contribution integration limits longitude (°) |
|---|---|---|---|---|---|---|---|---|---|---|
| MJO | −20, 20 | 30, 240 | All year | 13.46 | 20 | 100 | 164, 427 | Phases 1–8 | −20, 20 | 30, 240 |
| ER | −20, 15 | 120, 220 | Nov–Mar | 12.53 | 10 | 60 | 117, 176 | Phases 1–8 | −20, 15 | 120, 220 |
| EPEW | 2.5, 20 | 225, 265 | Jun–Oct | 12.91 | 2 | 10 | 127, 190 | Phases 1–8 | 2.5, 20 | 225, 265 |
| AEW | 0, 20 | 300, 360 | Jul–Sep | 13.86 | 2.5 | 20 | 86, 100 | Phases 1–8 | 0, 20 | 300, 360 |
| KW | −15, 15 | 130, 220 | All year | 13.22 | 2 | 6 | 309, 404 | Phases 1–8 | −15, 15 | 130, 220 |
| MRG | −15, 20 | 130, 200 | All year | 13.48 | 2.5 | 12 | 314, 374 | Phases 1–8 | −15, 15 | 130, 200 |

divided into eight phases, each spanning 45° of PC phase space. Composites for each of the eight phases were calculated by selecting days within that phase space where the index magnitude exceeded a value of 2. Conclusions of this study are not sensitive to the threshold chosen. To isolate the variability of interest, both TRMM 3B42 and $r$-diagnosed precipitation were bandpass filtered to time scales relevant to the CCEW in question before being composited over the days selected by the EOF index. The time scales used for bandpass filtering are given in Table 1, as are the number of days included within each phase composite.

A brief description of each EOF is provided here, and references describing detailed methodologies are provided for the interested reader. For each phenomenon, the first two EOFs are well separated from higher modes by the criteria of North et al. (1982), and EOF structures are similar to the composite structures presented in Figs. 2–7, and are therefore not reproduced here. The filtered MJO OLR (FMO) (Kiladis et al. 2014) index, based on 20–96-day bandpass-filtered OLR, was used for the MJO. The EOFs for MRGs were calculated using 2–10-day westward-only-filtered precipitation limited to 20°N–15°S, 130°E–160°W, as in Kiladis et al. (2009). The EOFs for KWs were calculated using wavenumber–frequency-filtered KW precipitation (following Kiladis et al. 2009) limited to 15°N–15°S, 130°E–140°W. The EOFs for EPEWs were calculated using June to October 2.5–12-day bandpass-filtered relative vorticity (calculated from horizontal winds) limited to 20°–2.5°N, 135°–95°W, similar to Rydbeck and Maloney (2014), except that no removal of tropical cyclones was performed here. The resulting composite evolution of east Pacific easterly waves (EPEWs) is very similar to Rydbeck and Maloney (2014, 2015). The EOFs for African easterly waves (AEWs) were calculated using July to September 2–6-day bandpass-filtered precipitation limited to 20°N–0°, 40°W–40°E, similar to that in Cheng et al. (2019). The EOFs for ERs were calculated using November to March 10–60-day westward-filtered precipitation limited to 20°N–20°S, 120°E–60°W.

### c. Basepoint compositing

To confirm the robustness to the results of the EOF composites, we provide a complimentary analysis using an alternative "basepoint" compositing method. At a given location (i.e., basepoint), standardized time series of precipitation that had been wavenumber–frequency filtered to the CCEW of interest were created. The wavenumber–frequency filtering windows used were the same as Kiladis et al. (2009), with the MJO filter retaining 20–100-day time scales and eastward wavenumbers 1–5. From this time series, maxima exceeding

TABLE 2. Details of the geographical locations and seasons used in the calculation of *r*-diagnosed precipitation for the basepoint composites, and the number of days included in the composites. Limits of integration used in the fractional contribution analysis described in section 3b are also provided.

| | Curve-fitting latitude (°) | Curve-fitting longitude (°) | Curve-fitting season | $a$ parameter | Bandpass-filtering high-frequency time scale (days) | Bandpass-filtering low-frequency time scale (days) | Min/max days in composite | Fractional contribution integration limits time (days) | Fractional contribution integration limits latitude (°) | Fractional contribution integration limits longitude (°) |
|---|---|---|---|---|---|---|---|---|---|---|
| MJO | −20, 20 | 30, 240 | All year | 13.46 | 20 | 100 | 33 | −14: 0.25: 14 | −20, 20 | 30, 240 |
| ER | 0, 15 | 120, 180 | All year | 14.49 | 10 | 60 | 72 | −6: 0.25: 6 | 0, 15 | 120, 180 |
| KW | 0, 15 | 120, 180 | All year | 14.49 | 2.5 | 20 | 166 | −2: 0.25: 2 | 0, 15 | 120, 180 |
| MRG | 0, 15 | 120, 180 | All year | 14.49 | 3 | 8 | 289 | −2: 0.25: 2 | 0, 15 | 120, 180 |

plus-one standard deviation were selected to isolate strong convective events associated with each wave passage. Maxima were required to be separated by a number of days greater than the longest time scales typically associated with the CCEW in question (e.g., at least 100 days for the MJO) to ensure that separate events were chosen. This time scale is equivalent to the low-frequency time scale used for bandpass filtering, given in Table 2. As this may exclude events that occur in rapid succession (e.g., successive MJO events), a lower magnitude threshold of plus-one standard deviation was used in order to maintain an adequate sample size. Lag-day composites were then made based around "day 0," the maxima of the time series. To isolate the variability of interest, both TRMM 3B42 and *r*-diagnosed precipitation were bandpass filtered to time scales relevant to the CCEW in question before being composited over the days selected by the basepoint index. The time scales used for bandpass filtering are given in Table 2, as are the number of days included within each composite.

## 3. The role of moisture in convective coupling

In this section, we compare *r*-diagnosed precipitation, whose only source of variability is CSF, to TRMM 3B42 precipitation, which contains the full spectrum of variability arising from the myriad of processes driving precipitation. Similarities and differences between the two datasets provide insight to the role that moisture variations play in driving precipitation variations.

### a. Comparing basic features of r-diagnosed precipitation and observed precipitation

Figures 1a and 1b show raw power spectra of TRMM and *r*-diagnosed precipitation, respectively, where *r*-diagnosed precipitation has been calculated using data limited to tropical (15°N–15°S) oceans. At higher frequencies and larger wavenumbers (i.e., smaller spatial scales), *r*-diagnosed precipitation has much less power than TRMM precipitation, indicating that much of the variability in TRMM precipitation at these spatiotemporal scales cannot be explained by variations in CSF. At larger spatiotemporal scales (i.e., the spectral regions associated with the MJO and Rossby waves) power of *r*-diagnosed precipitation is similar to that of TRMM precipitation, suggesting that moisture variations at these scales have the potential to explain a higher proportion of precipitation variability. Cross-spectra of TRMM and *r*-diagnosed precipitation were calculated using the methodology of Wheeler and Kiladis (1999), who used this approach to diagnose the relationship between outgoing longwave radiation and MSU satellite temperature. These spectra (Figs. 1c,d) indicate high coherence-squared values that
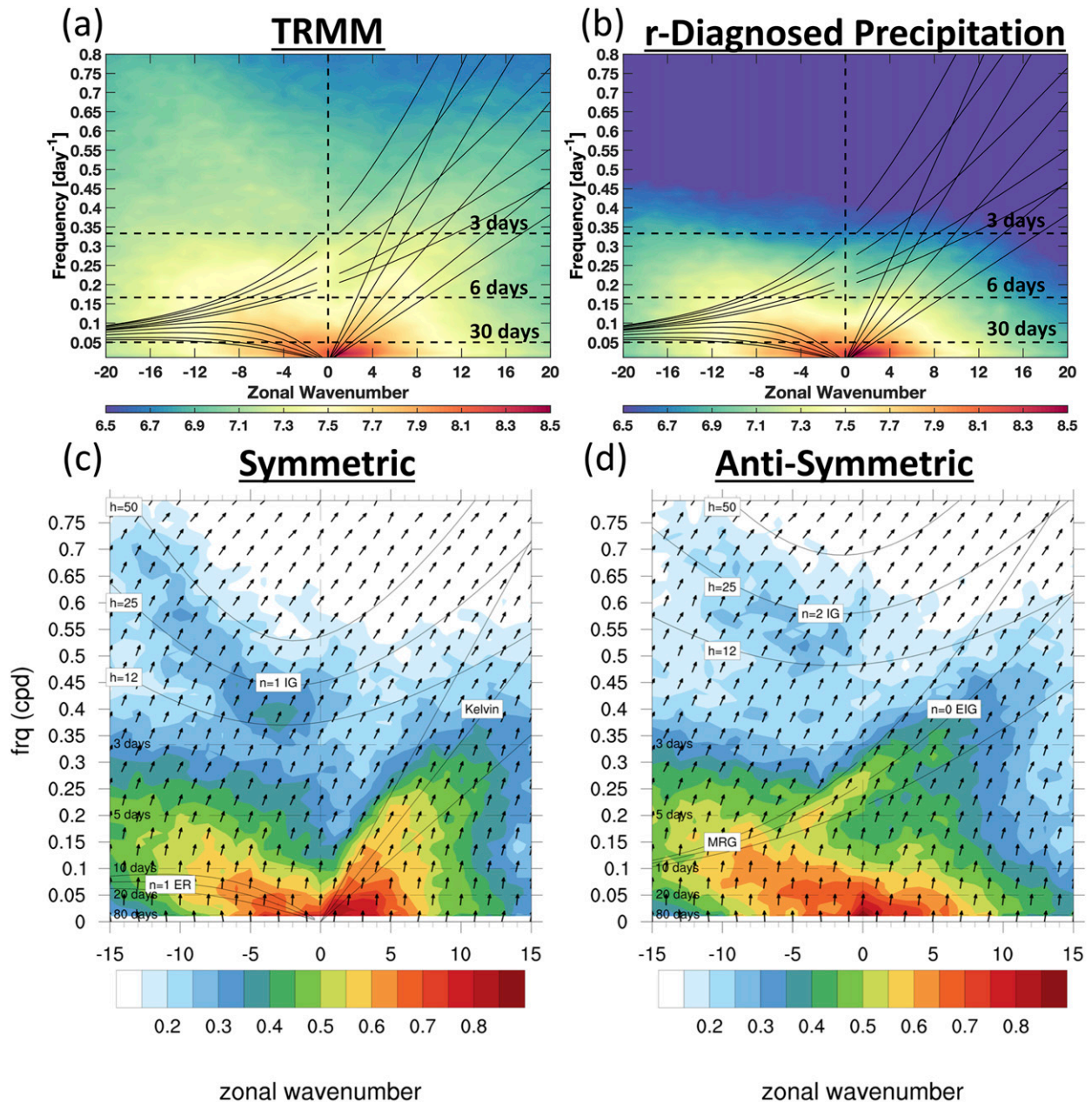
FIG. 1. Log$_{10}$ power spectra of (a) 6-hourly 15°N–15°S TRMM precipitation and (b) $r$-diagnosed precipitation produced by inputting ERAi CSF to Eq. (1), using $a_d$ and $r_d$ parameters obtained from the curve fitting of 6-hourly TRMM precipitation and ERAi CSF. (c) Symmetric and (d) antisymmetric cross-spectra of TRMM precipitation and $r$-diagnosed precipitation, where color shading and contours indicate coherence squared and the arrows indicate phase. Arrows pointed upward indicate an in-phase relationship, arrows pointed upward and slightly to the right indicate that TRMM precipitation leads $r$-diagnosed precipitation slightly. Dispersion curves for the Kelvin, $n = 1$ equatorial Rossby, $n = 0$ eastward inertio-gravity, and mixed Rossby–gravity waves are plotted for equivalent depths of 8, 12, 25, 50, and 90 m in (a) and (b). Additional dispersion curves for $n = 1$ and $n = 2$ westward inertio-gravity waves are included in (c) and (d), respectively, and equivalent depths in these plots are 12, 25, and 50 m. Spectra are calculated using overlapping 96-day subsets, following the methodology of Wheeler and Kiladis (1999).

exceed 0.85 and 0.7 near the MJO and Rossby wave portions of the spectra, respectively. Not only does $r$-diagnosed precipitation produce the correct amount of variability at these spatiotemporal scales, but also the correct timing of

this variability, with a nearly in phase relationship (upward-pointed arrows) between CSF and precipitation, as has been shown in past studies (e.g., Wolding and Maloney 2015). Moving to higher frequencies and larger

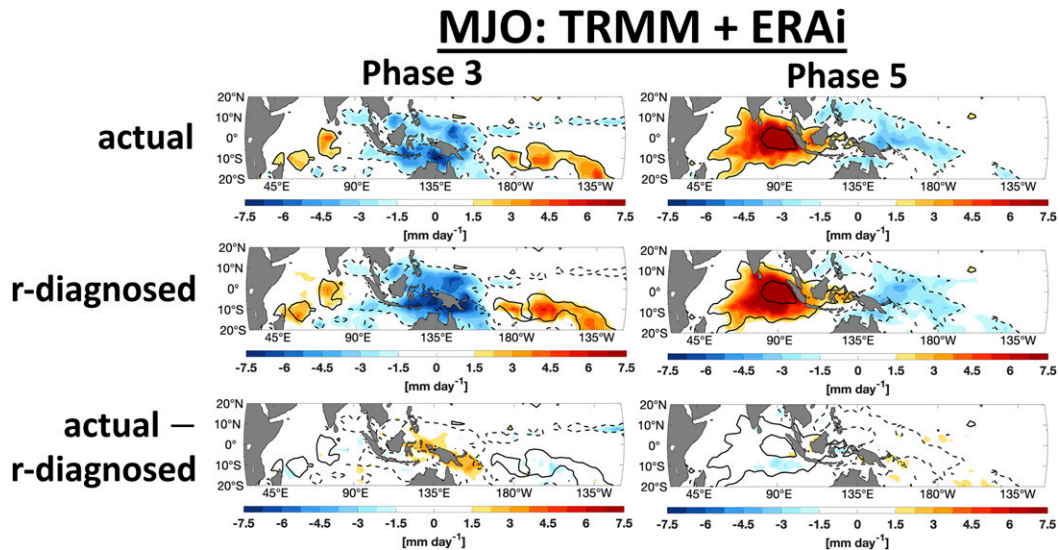# MJO: TRMM + ERAi

## Phase 3    Phase 5



FIG. 2. Composite Madden–Julian oscillation (MJO) precipitation anomalies for two phases that together provide a representative sampling of the MJO life cycle. Color shading indicates (top) TRMM precipitation, (middle) precipitation diagnosed using Eq. (1) (*r* diagnosed), and (bottom) the difference between TRMM precipitation and *r*-diagnosed precipitation (i.e., the error). TRMM precipitation is contoured at 1.5, 7.5, 15, 30, and 60 mm day$^{-1}$ in all plots to aid comparison, with positive and negative anomalies in solid and dashed contours, respectively. Composites are produced using the EOF-based methodology described in section 2. The number of days included in the composites are provided in Table 1. Resulting values of fractional contribution are provided in Table 3.

wavenumbers, coherence steadily declines and *r*-diagnosed precipitation begins to lag observed precipitation by a small amount (i.e., vectors pointed upward and slightly to the right). Regions of enhanced coherence are evident along dispersion curves of MRGs and lower-frequency Kelvin waves. Along the Kelvin wave dispersion curves, coherence decreases smoothly when moving to higher frequencies. Taken together, these results suggest that variations in CSF have the potential to explain a larger fraction of precipitation variability at larger/longer spatiotemporal scales.

## b. The MJO

The MJO is the leading mode of tropical intraseasonal variability, and thorough reviews of the MJO are provided by Zhang (2005) and Lau and Waliser (2012). The features of the MJO most relevant to this study are its intraseasonal (20–100-day) time scale, large spatial scale (wavenumbers 1–3), the applicability of WTG balance to the MJO, and the important role moisture plays in both theories and observations of the MJO (Sobel et al. 2001; Raymond 2001; Khouider and Majda 2008; Adames and Kim 2016; Wolding and Maloney 2015; Wolding et al. 2016, 2017).

Figure 2 shows composite MJO precipitation anomalies for two phases that together provide a representative sampling of the MJO life cycle. Color shading indicates TRMM precipitation (top row), precipitation

diagnosed using Eq. (1) (second row, *r*-diagnosed precipitation), and the difference between TRMM precipitation and *r*-diagnosed precipitation (i.e., the "error," bottom row). TRMM precipitation is contoured in all plots to aid comparison. Visual inspection shows that *r*-diagnosed precipitation closely matches TRMM precipitation in distribution, magnitude, and evolution throughout the MJO life cycle.

To objectively assess the ability of *r*-diagnosed precipitation $P_d$ to capture the magnitude, geographical distribution, and evolution of observed precipitation $P$ throughout the life cycle of various CCEWs, we use the fractional contribution (hereafter FC) (Andersen and Kuang 2012; Arnold et al. 2015), which is given by

$$\mathrm{FC} = \frac{\iiint P_d(x,y,t)P(x,y,t)\,dx\,dy\,dt}{\iiint P^2(x,y,t)\,dx\,dy\,dt}. \qquad (3)$$

If *r*-diagnosed precipitation accurately reproduces the magnitude, distribution, and evolution of observed precipitation throughout the life cycle of a CCEW, the fractional contribution will be close to 1. If *r*-diagnosed precipitation poorly reproduces the characteristics of observed precipitation, the fractional contribution will be closer to 0. The limits of integration in time, latitude, and longitude for EOF and basepoint composites are

TABLE 3. Fractional contribution (FC) values for EOF and basepoint composite analyses. As detailed in section 3b, FC is used to objectively assess the ability of $r$-diagnosed precipitation [see Eq. (1)] to capture the magnitude, geographical distribution, and evolution of TRMM 3B42 precipitation throughout the life cycle of various CCEWs. The top row shows the FC of $r$-diagnosed precipitation, and the bottom row shows the FC of the difference between TRMM precipitation and $r$-diagnosed precipitation (i.e., the error).

| | MJO | | ER | | EPEW | | AEW | | KW | | MRG | |
|---|---|---|---|---|---|---|---|---|---|---|---|---|
| | EOF | Basepoint | EOF | Basepoint | EOF | Basepoint | EOF | Basepoint | EOF | Basepoint | EOF | Basepoint |
| $r$ diagnosed | 1.03 | 0.89 | 0.79 | 0.82 | 0.76 | N/A | 0.52 | N/A | 0.53 | 0.49 | 0.51 | 0.52 |
| Actual − $r$ diagnosed | −0.03 | 0.11 | 0.21 | 0.18 | 0.24 | N/A | 0.48 | N/A | 0.47 | 0.51 | 0.49 | 0.48 |

provided in Tables 1 and 2, respectively. Resulting fractional contribution values are provided in Table 3. Note that land areas are excluded during the calculation of FC.

When calculated over the MJO life cycle in the EOF and basepoint composites (not shown), the FC of $r$-diagnosed precipitation is 1.03 and 0.89, respectively (Table 3). These results support the previous assertion that $r$-diagnosed precipitation captures the distribution, magnitude, and evolution of precipitation throughout the MJO life cycle, and suggest that MJO precipitation is primarily modulated by variations in moisture, consistent with observations and moisture-mode theories of the MJO (e.g., Raymond and Fuchs 2009; Powell and Houze 2015; Adames and Kim 2016)

### c. Equatorial Rossby waves

ERs are westward-propagating gyres symmetric about the equator (see Kiladis et al. 2009). The features of ERs most relevant to this study are their 10–40-day time scale, strong rotational character, and that they have a dry analytical analog whose circulation is weakly divergent (Matsuno 1966). We note the similar power of, and large degree of coherence between, $r$-diagnosed precipitation and TRMM precipitation in the ER region of the spectrum (Fig. 1). Considering also the apparent applicability of WTG balance to ERs, and the scaling results of Adames et al. (2019), one might expect the modification of the moist environment to be the primary mechanism by which the circulation of ERs modulates convection (Wolding et al. 2016; Gonzalez and Jiang 2019).

Figure 3 shows composite ER precipitation anomalies for two phases that together provide a representative sampling of the ER life cycle. Visual inspection shows that $r$-diagnosed precipitation matches TRMM precipitation in distribution, magnitude, and evolution fairly well throughout the ER life cycle, though to a lesser degree than was seen for the MJO. The FC is 0.79 and 0.82 when calculated using EOF and basepoint composites, respectively (Table 3). The difference between TRMM and $r$-diagnosed precipitation (bottom row) shows that $r$-diagnosed precipitation underestimates the

magnitude of the largest precipitation anomalies. Consistent with the findings of Gonzalez and Jiang (2019), these results suggest ER precipitation is primarily modulated by variations in moisture, and that other coupling mechanisms are playing important secondary roles.

### d. Easterly waves

Westward-propagating synoptic-scale rotational disturbances exist in a variety of locations under a variety of names [e.g., easterly waves, tropical depression (TD)-type disturbances, synoptic-scale monsoonal disturbances], reflecting their diverse characteristics and broad spectrum of energy sources. Here we focus on EWs, for which overviews are provided by Kiladis et al. (2006) and Serra et al. (2008). The features of EWs most relevant to this study are their 2.5–12-day time scale, synoptic spatial scale, and that they do not have a dry analytical analog (Matsuno 1966). Here we analyze two types of EWs that occupy somewhat different portions of the energy source spectrum, EPEWs and AEWs.

While convection and barotropic conversions serve as important energy sources for both AEWs and EPEWs, convection is thought to make up a larger proportion of the energy source of EPEWs (Lau and Lau 1992; Rydbeck and Maloney 2015). The presence of a strong meridional temperature gradient and attendant easterly jet over north Africa provides large sources of baroclinic and barotropic energy for AEWs (Thorncroft and Hoskins 1994a,b; Kiladis et al. 2006). AEWs also appear to have stronger adiabatically forced vertical motion (i.e., vertical motion forced by EW dynamics not dependent on convection) than EPEWs. Kiladis et al. (2006) and Rydbeck and Maloney (2015) used Q-vector divergence to estimate adiabatically forced vertical motion in AEWs and EPEWs, respectively. AEWs were found to have adiabatically forced vertical motion slightly leading convection over west Africa, while adiabatically forced vertical motion was roughly in quadrature with EPEW convection, leading convection by a quarter cycle. Rydbeck and Maloney (2015) also showed that EPEW convection was coincident with anomalous column moisture, and suggested that column moisture largely determined the preferred evolution of convection throughout the EPEW life cycle.
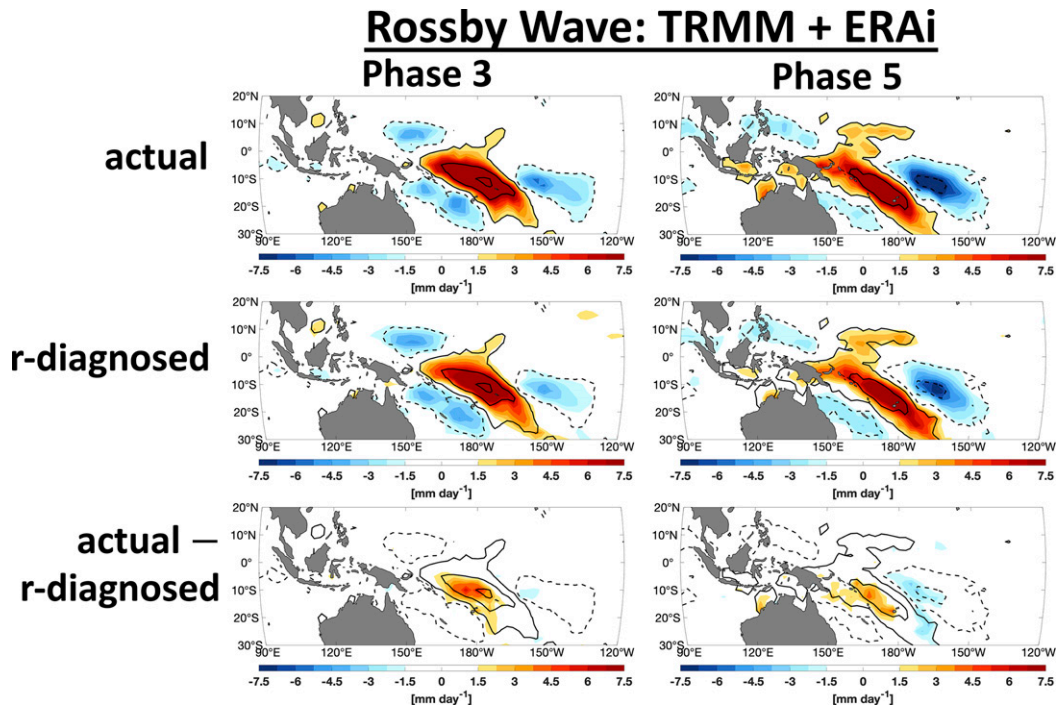
FIG. 3. As in Fig. 2, but for equatorial Rossby waves. Data were restricted to boreal winter months of November–March in the calculation of r-diagnosed precipitation.

Figure 4 shows composite EPEW precipitation anomalies for two phases that together provide a representative sampling of the EPEW life cycle. The r-diagnosed precipitation and TRMM precipitation are fairly similar in distribution, magnitude, and evolution throughout the EPEW life cycle, producing a FC of 0.76 in the EOF composites (Table 3). The difference between TRMM and r-diagnosed precipitation (bottom row) shows the degree to which r-diagnosed precipitation underestimates the magnitude of the largest precipitation anomalies.

Figure 5 shows composite AEW precipitation anomalies for two phases that together provide a representative sampling of the AEW life cycle. The r-diagnosed precipitation both underestimates the magnitude of, and slightly lags, TRMM precipitation anomalies, having a FC of only 0.52 when calculated for oceanic regions only in the EOF composites (Table 3). Over Africa, r-diagnosed precipitation captures almost none of the anomalies seen in TRMM precipitation. An important caveat to this is that we are using an oceanic CSF–precipitation curve (i.e., $a_d$ calculated for oceanic precipitation) to do this diagnosis, though $a_d$ over land is much less than over the ocean (Ahmed and Schumacher 2015), so if anything the use of the larger oceanic $a_d$ should result in an overdiagnosis of precipitation over land. As convection moves offshore, the diagnosed precipitation

begins to more closely match TRMM precipitation, though it continues to underestimate the magnitude of the anomalies and lag TRMM precipitation slightly. The phasing between the diagnosed precipitation error and TRMM precipitation (bottom row) is similar to the phasing between the adiabatically forced vertical motion and convection documented by Kiladis et al. (2006, see their Figs. 3 and 14).

In agreement with previous studies, these results suggest adiabatically driven wave motions are a more important convective coupling mechanism for AEWs than for EPEWs, whose convection appears to be modulated by moisture to a larger degree (Kiladis et al. 2006; Rydbeck and Maloney 2015).

*e. Kelvin waves*

KWs are eastward-propagating equatorially symmetric phenomena, and a thorough review is provided by Kiladis et al. (2009). The features of KWs most relevant to this study are their 2.5–20-day time scale, their gravity wave characteristics, and that they have a dry analytical analog whose circulation is strongly divergent (Matsuno 1966; Adames et al. 2019; Yasunaga et al. 2019).

Figure 6 shows composite KW precipitation anomalies for two phases that together provide a representative sampling of the KW life cycle. While r-diagnosed precipitation has a distribution and evolution very
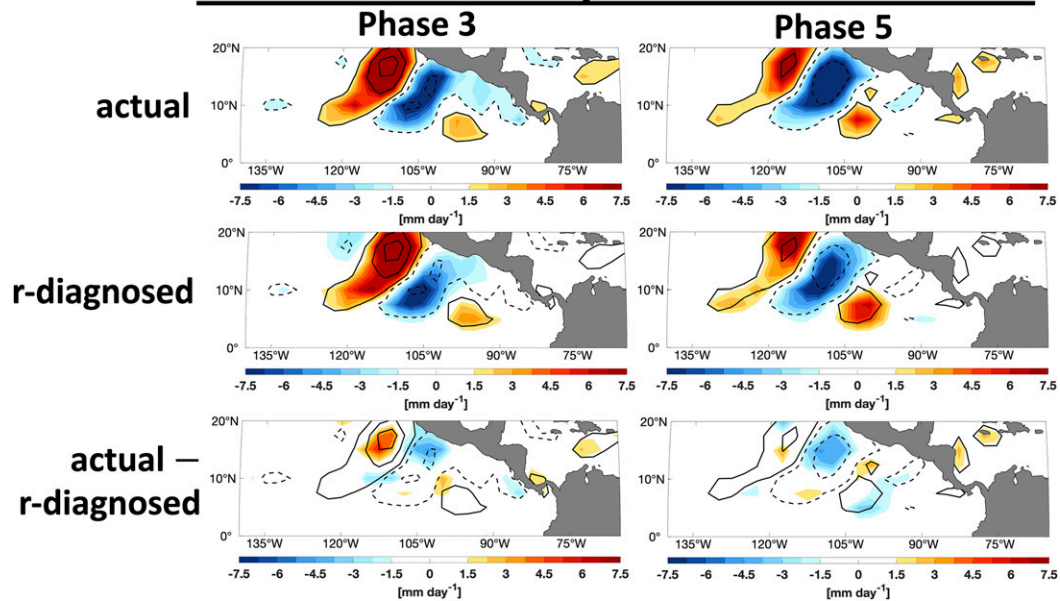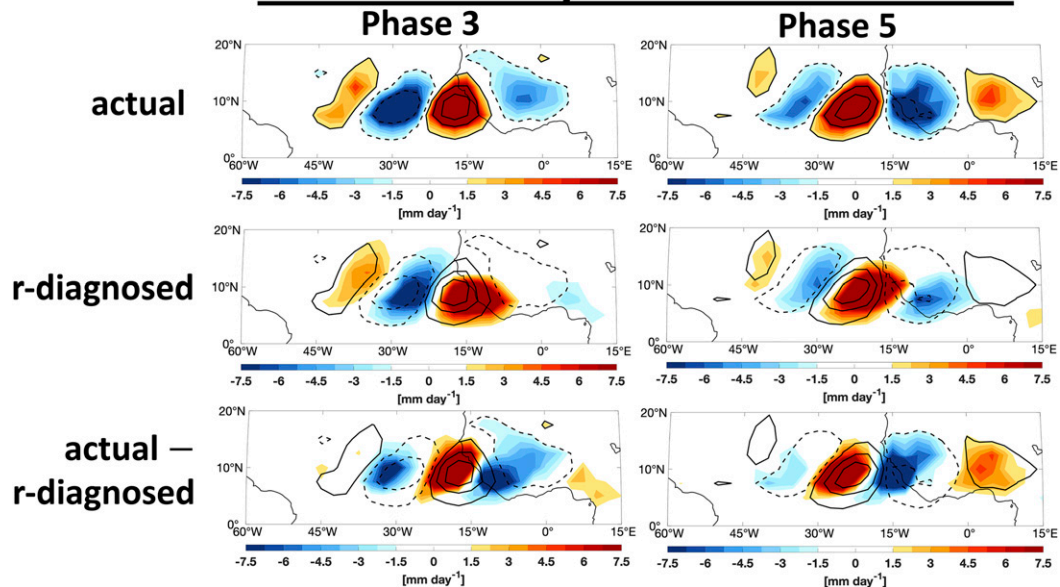
## East Pacific Easterly Wave: TRMM + ERAi



FIG. 4. As in Fig. 2, but for east Pacific easterly waves. Data were restricted to boreal summer months of June–October in the calculation of *r*-diagnosed precipitation.

similar to TRMM precipitation, it underestimates the magnitude of the anomalies, having FCs of 0.53 and 0.49 for EOF and basepoint composites, respectively (Table 3). That *r*-diagnosed precipitation gets approximately the correct phasing but underestimates the magnitude of precipitation anomalies to such a large degree suggests that other mechanisms are playing primary roles in convective coupling, and acting cooperatively with moisture variations to modulate precipitation.

## African Easterly Wave: TRMM + ERAi



FIG. 5. As in Fig. 2, but for African easterly waves. Data were restricted to boreal summer months of July–September in the calculation of *r*-diagnosed precipitation.
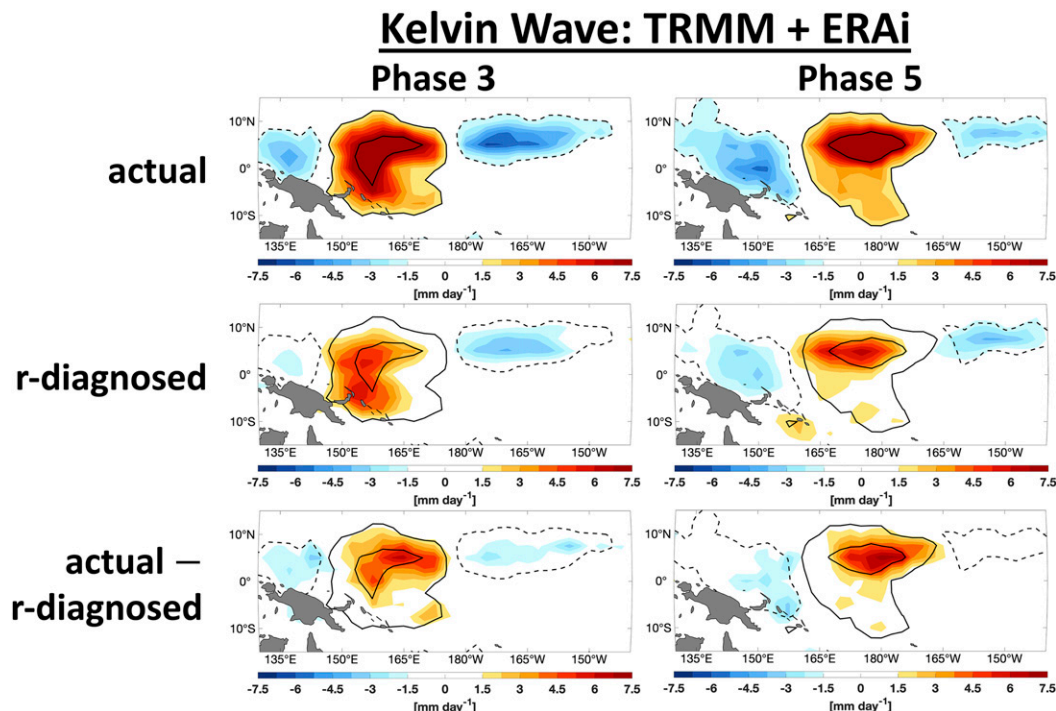
FIG. 6. As in Fig. 2, but for Kelvin waves.

### f. Mixed Rossby–gravity waves

MRGs are westward-propagating equatorial waves, and reviews of MRGs are provided by Kiladis et al. (2016) and Dias and Kiladis (2016). The features of MRGs most relevant to this study are their 2–10-day time scale, mixed rotational and gravity wave characteristics, and that they have a dry analytical analog whose circulation has strong divergence antisymmetric about the equator (Matsuno 1966). Given the mixed rotational and gravity wave characteristics of MRGs, it is more difficult to make an a priori hypothesis as to whether modification of the moist environment will serve as the primary convective coupling mechanism. Cross-spectra of r-diagnosed precipitation and TRMM precipitation exhibit considerable coherence in the MRG band (Fig. 1), although this coherence is weaker than in the ER and MJO bands. Kiladis et al. (2016) demonstrate how the divergent part of MRG circulations is relatively weak compared to that of EIGs, though it is stronger than that of ERs. The scaling of Adames et al. (2019) indicates that MSE fluctuations in MRGs should be largely driven by temperature fluctuations, suggesting that such fluctuations could be an important convective coupling mechanism for MRGs.

Figure 7 shows composite MRG precipitation anomalies for two phases that together provide a representative sampling of the MRG life cycle. Here we have chosen a particularly interesting geographic region to examine MRGs, which has been highlighted by several studies as a region where MRGs often transition to TD-type disturbances (Lau and Lau 1992; Dickinson and Molinari 2002; Kiladis et al. 2009). The structure of the MRG is evident east of ~155°E, confirmed by the appearance of an antisymmetric precipitation signal about the equator in Fig. 7, and through examination of meridional winds (not shown). The northern convective branch of this structure transitions rather quickly to the SW–NE-tilted structure of a TD-type disturbance as it moves westward of ~150°E. While r-diagnosed precipitation has a distribution and evolution similar to TRMM precipitation, it underestimates the magnitude of the anomalies, having fractional contributions of 0.51 and 0.52 for EOF and basepoint composites, respectively (Table 3). Similar to KWs, other mechanisms appear to be playing primary roles in convective coupling, and acting cooperatively with moisture variations to modulate precipitation

### 4. The role of adiabatically driven wave motions in convective coupling

Results of section 3 suggest that moisture variations and some other coupling mechanism(s) are working
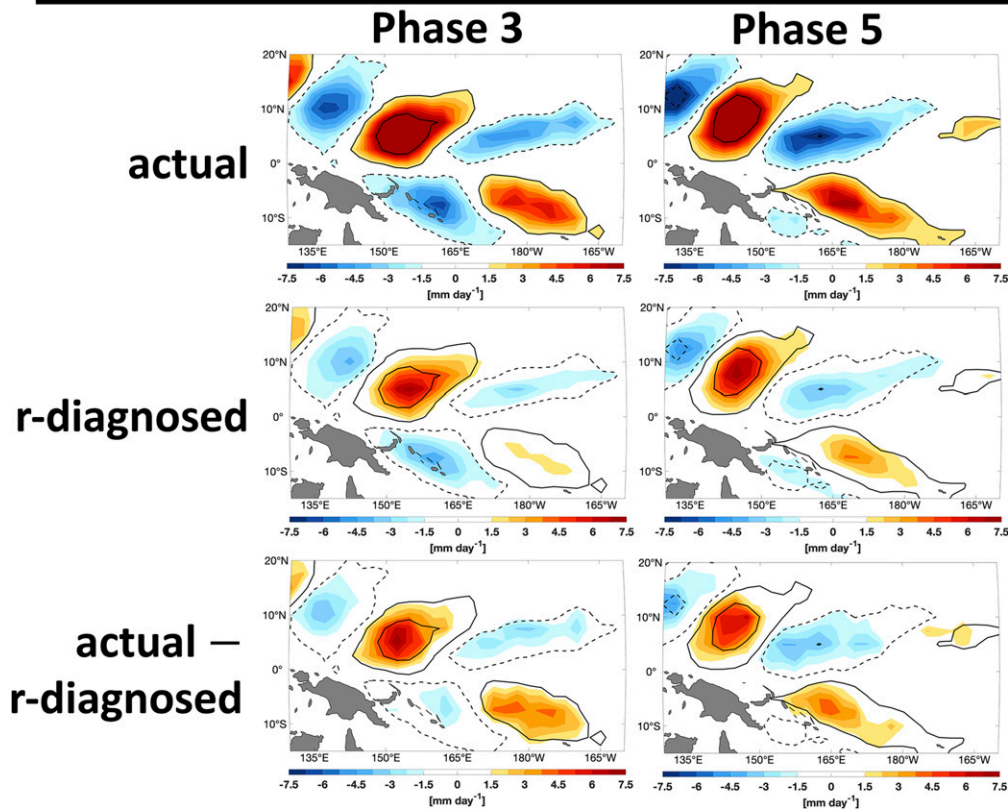
FIG. 7. As in Fig. 2, but for mixed Rossby–gravity waves. Note that the structure of the MRG is evident east of ~155°E (confirmed through examination of meridional winds; not shown), and the northern convective branch of this structure transitions rather quickly to the SW–NE-tilted structure of a TD-type disturbance as it moves west of ~150°E.

cooperatively to modulate precipitation in KWs and MRGs. Here we provide supporting evidence for this assertion, using a methodology that is independent of that used in the previous section.

### a. Linearization of CSF–precipitation relationship

To consider how CSF variations associated with CCEWs impact precipitation as they propagate through a "slowly" varying background, we follow Adames (2017), and linearize Eq. (1) using a Taylor series expansion truncated at the second term:

$$P_d(r) \simeq \overline{P_d}(\overline{r}) + r' \frac{\partial P_d}{\partial r}\bigg|_{r=\overline{r}}. \qquad (4)$$

Here the overbar denotes the slowly varying background, which is composed of the mean as well as slow variations such as those associated with the seasonal cycle and interannual variability. The prime denotes variations from this slowly varying background, occurring on time scales of the CCEW itself (e.g., 20–100-day

variations for the MJO). Equation (4) can be rewritten as

$$P_d(r) \simeq \overline{P_d}(1 + a_d r'), \qquad (5)$$

which can be rearranged to solve for precipitation variations as a function of CSF variations:

$$P'_d(r') \simeq a_d \overline{P} r'. \qquad (6)$$

Equation (6) states that precipitation variations are proportional to variations in CSF, scaled by $a_d$ and the background precipitation rate; $a_d$ serves as a measure of the sensitivity of precipitation to variations in CSF, and is inversely proportional to the convective moisture adjustment time scale $\tau_c$, the time scale by which moisture and precipitation are relaxed toward their "background" state (Bretherton et al. 2004; Adames 2017; Rushley et al. 2018). The larger $a_d$, the larger the precipitation response to a variation in CSF, and the more quickly this relaxation occurs.

## b. Sensitivity of precipitation to variations in CSF

Equation (6) can be rearranged to make a diagnostic equation for $a_d$:

$$a_d = \frac{\left(\frac{P'}{\overline{P}}\right)}{r'}, \qquad (7)$$

where $a_d$ measures the sensitivity of precipitation (normalized by the background precipitation rate) to variations in CSF. Equation (7) was used to diagnose $a_d$ in wavenumber–frequency space using the following methodology. The 6-hourly TRMM 3B42 precipitation and ERAi CSF data were limited to 15°N–15°S and separated into 68 subsets of length 96 days. The 96-day time-mean precipitation rate of each subset was calculated at each location and saved to be used as $\overline{P}$ in Eq. (7). FFTs were performed in both time and space, and data were limited to a single wavenumber–frequency combination by setting all other spectral coefficients to zero. Data were then transformed back to physical space, giving precipitation and CSF anomalies $P'$ and $r'$, respectively, and limited to oceanic regions where climatological precipitation exceeds 5mm day$^{-1}$. At each location the precipitation anomaly $P'$ was divided by the $\overline{P}$, yielding values of $P'/\overline{P}$ at each location, collocated with CSF anomalies ($r'$). To avoid "divide by zero" errors in using Eq. (7), we then binned the numerator $P'/\overline{P}$ by the denominator $r'$, where $r'$ was been separated into 100 bins of equal width spanning the range of $r'$. We calculated the bin-mean value of $P'/\overline{P}$ for all bins with more than 16 000 observations, and then least squares fit a linear relationship to this bin-mean value, and the slope of this line gave our desired parameter $a_d$. We performed this iteratively over all wavenumber–frequency combinations, and verified that the resulting relationship between $P'/\overline{P}$ and $r'$ is indeed linear for several regions of wavenumber–frequency space, including those associated with Kelvin waves and the MJO. This approximately linear behavior is expected, given the small perturbations that result from filtering to retain only a single wavenumber–frequency combination at a given time. Several different binning thresholds were tested, and results discussed below were not found to be sensitive to the different thresholds.

Figure 8 is a wavenumber–frequency diagram of the $a_d$ parameter, and shows that $a_d$ is much larger in regions of the spectrum associated with KWs, EIGs, and WIGs than other regions of the spectrum. Kiladis et al. (2009) showed that peak modulation of convection by MRGs occurs near wavenumber 1 of the spectrum, and inspection of Fig. 8 suggests some modification of $a_d$ in this region as well. These results indicate that variations in CSF are associated with disproportionally large precipitation
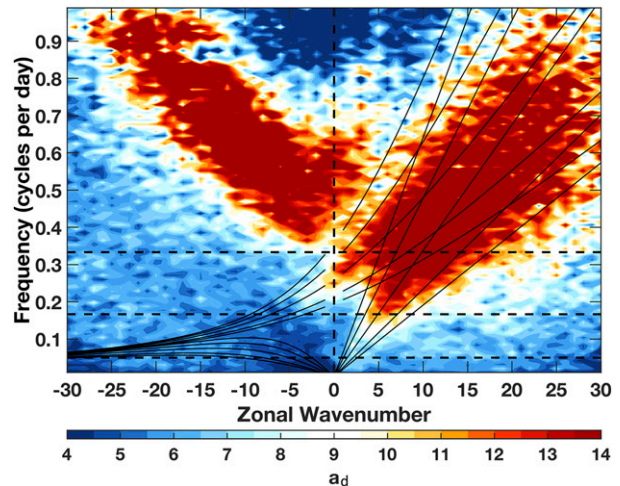


FIG. 8. Wavenumber–frequency diagram of the $a_d$ parameter, where Eq. (7) has been used to diagnose $a_d$ using TRMM precipitation and ERAi CSF. Data were limited to tropical (15°N–15°S) oceanic regions where climatological precipitation exceeded 5 mm day$^{-1}$. Further details of the methodology are provided in section 4.

responses in KWs, EIGs, WIGs, and, to a lesser degree, MRGs. Again, this suggests that other processes are acting cooperatively with moisture variations to modulate precipitation. One interesting result of this cooperative modulation of precipitation is that it shortens $\tau_c$, allowing moisture anomalies to be removed more rapidly. By accelerating the removal of moisture, these phenomena may be allowing temperature to assume a more important role in driving moist static energy fluctuations, and self-promoting their own gravity wave character.

## c. Modulation of the thermodynamic environment by adiabatically driven wave motions

Here adiabatically driven wave motions refers to motions arising from wave dynamics not dependent on convection, sometimes referred to as "dry dynamics," such as those that arise in the shallow-water equations of Matsuno (1966). A real-world example of such adiabatically driven motions are the circulations of MRGs in the stratosphere, which are not coupled to convection (e.g., Kiladis et al. 2016). KWs, EIGs, and WIGs have gravity wave characteristics with large equatorial wave dynamic driven vertical velocities. Wolding et al. (2016) showed that, unlike anywhere else in wavenumber–frequency space, adiabatic cooling commonly exceeds apparent heating $Q_1$ by up to 10% in regions of the spectrum associated with KWs, EIGs, and WIGs (see their Fig. 24). Such strong adiabatically forced upward motion could serve to reduce static stability and convective inhibition, helping create and/or maintain a
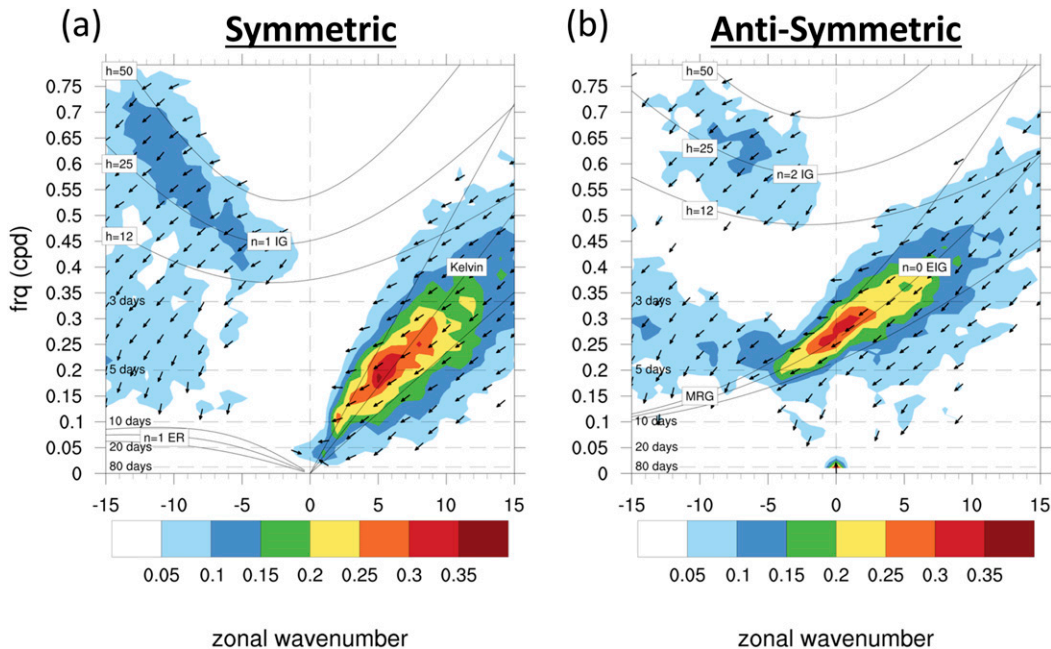
FIG. 9. (a),(b) As in Figs. 1c and 1d, respectively, but for cross-spectra of TRMM precipitation and ERAi column-integrated dry static energy (DSE) interpolated to a horizontal grid of 1.5° × 1.5° for the time period of 1998–2012. The mass-weighted vertical integral is from 1000 to 100 hPa. Arrows pointed downward indicate an out-of-phase relationship; arrows pointed downward and slightly to the left indicate that maxima in TRMM precipitation lead minima in DSE by approximately one-eighth of a cycle.

more favorable environment for convection (Mapes 2000; Tulich and Mapes 2010; Fuchs et al. 2014). This large-scale vertical motion will also act to moisten the column via large-scale vertical moisture advection, serving as a cooperative mechanism that could strongly modulate convection. Note that this strong equatorial wave driven vertical motion differs from the vertical motion in WTG phenomena like the MJO, which is better viewed as a comparatively slow and delayed gravity wave adjustment to apparent heating. As the latter vertical motion can be understood as an adjustment to WTG, the corresponding adiabatic cooling can at most balance, but not exceed, apparent heating, and therefore cannot further destabilize the environment beyond its WTG state.

If such mechanisms were at work, one would expect to see a coherent modulation of dry static energy (DSE), with the minima of DSE slightly lagging the maxima in precipitation. Cross-spectra of TRMM precipitation and ERAi column-integrated (1000–100 hPa) DSE interpolated to a horizontal grid of 1.5° × 1.5° for the time period of 1998–2012 were calculated following the methodology of Wheeler and Kiladis (1999). Inspection of the cross-spectra, presented in Fig. 9, shows regions of enhanced coherence in the KW (Fig. 9a) and MRG to n = 0 EIG transition (Fig. 9b) regions of the spectrum. There is also enhanced, albeit weaker, coherence in the WIG and EW

regions of the spectrum. Arrows indicate that maxima in precipitation occur approximately an eighth of a cycle before minima in DSE. This is consistent with the findings of Yasunaga et al. (2019), who showed that vertical advection damps column moist static energy anomalies in these wave modes. Evaporation of stratiform precipitation cooling the lower troposphere (i.e., further driving down $Q_1$) in the later stages of the convective life cycle may also be contributing to the lag in the relationship. Yasunaga and Mapes (2012) showed the second baroclinic (i.e., vertical dipole) heating component is especially prevalent in, and important to, more divergent wave types (cf. their Figs. 2c,d to our Figs. 9a,b). While results of idealized studies support the mechanistic narrative presented here, observational studies of these waves highlight their complicated structural evolution, emphasizing that a complex interplay between their circulations, thermodynamic environment, and convective heating lay at the heart of their convective evolution (Wheeler and Kiladis 1999; Mapes 2000; Straub and Kiladis 2003; Kuang 2008; Andersen and Kuang 2012; Yasunaga and Mapes 2012; Kiladis et al. 2016).

## 5. Discussion and conclusions

The coupling of large-scale circulations and convection is a defining characteristic of convectively coupled

equatorial waves (CCEWs), yet much remains to be learned about the mechanisms responsible for this coupling. This study has used the relationship between column saturation fraction (CSF) and precipitation to investigate the role of moisture in convective coupling. In doing so, we have come to the following main conclusions:

1) Modulation of large-scale moisture serves as the primary convective coupling mechanism for the MJO and, to a lesser degree, equatorial Rossby waves and east Pacific easterly waves.
2) Adiabatically driven wave motions appear to play a key role in the convective coupling of Kelvin waves, mixed Rossby–gravity waves, inertio-gravity waves, and African easterly waves.
3) CCEWs that behave more like gravity waves modify their own convective environment in a way that shortens the convective moisture adjustment time scale $\overline{\tau_c}$, potentially helping them promote their own gravity wave characteristics.

Each of these conclusions will now be discussed in turn.

The CSF–precipitation relationship was used to create a dataset of "diagnosed" precipitation, whose only source of variability is CSF. Diagnosed precipitation was compared to TRMM 3B42 precipitation, and shown to capture nearly all Madden–Julian oscillation (MJO)-related variability, ~80% of equatorial Rossby (ER) wave–related variability, and ~75% of east Pacific easterly wave (EPEW)-related variability. This suggests that moisture variations serve as a primary convective coupling mechanisms for these phenomena, and that secondary coupling mechanisms are important to ERs and EPEWs. In contrast, diagnosed precipitation was only able to explain roughly half of the precipitation variability associated with African easterly waves (AEW), Kelvin waves (KW), and mixed Rossby–gravity waves (MRG), suggesting that other convective coupling mechanisms are playing primary roles in these phenomena. These latter phenomena are known to have strong adiabatically forced vertical motions (i.e., motions driven by wave dynamics not dependent on convection), and we posit that this could serve to reduce static stability and convective inhibition while simultaneously moistening the column, creating a cooperative "1–2 punch" that fosters convection. In support of this narrative we presented cross-spectra of precipitation and column-integrated dry static energy, which exhibit enhanced coherence and a roughly out-of-phase relationship in the KW, MRG, and inertio-gravity wave regions of the spectrum. One interesting consequence of this cooperative modulation of precipitation is that it

shortens the convective moisture adjustment time scale $\overline{\tau_c}$, the time scale by which moisture and precipitation anomalies are relaxed toward their "background" state. By speeding the adjustment of moisture, and allowing temperature anomalies to play a more dominant role in driving MSE fluctuations, KWs, MRGs, and inertio-gravity waves may be self-promoting their own gravity wave character. These results are broadly consistent with the body of established literature on this topic (Mapes 2000; Sobel et al. 2001; Straub and Kiladis 2003; Kuang 2008; Khouider and Majda 2008; Yasunaga and Mapes 2012; Fuchs et al. 2014; Wolding et al. 2016; Adames and Ming 2018; Gonzalez and Jiang 2019), as well as the scaling results of Adames et al. (2019).

## a. Implications for model representation of CCEWs

A companion study, Part I, identified shortcomings in the model representation of moisture–convection coupling in several climate models, all implementing traditional convective parameterizations. Model representation of moisture–convection coupling was shown to be improved in a model implementing "superparameterization" (Grabowski 2001; Randall et al. 2003), which has also been shown to improve representation of the MJO (Benedict and Randall 2009). Results of this study provide additional insight to why realistic moisture–convection coupling may be a prerequisite for simulation of phenomena like the MJO, whose convective coupling appears to be achieved through a single mechanism, and may not be for other phenomena like Kelvin waves, whose convective coupling is achieved through multiple mechanisms (Hung et al. 2013; Ahn et al. 2017). Results of this study also motivate further development of process-level diagnostics that can be used to assess model representation of temperature–convection feedbacks, similar to those developed in Part I to assess moisture–convection feedbacks.

## b. Caveats and future directions

Two considerable caveats of this work warrant further discussion. First, Kelvin waves, MRGs, and inertio-gravity waves have vertical structures that are considerably more tilted than those of ERs and the MJO (Kiladis et al. 2009). While we have applied a consistent framework in an attempt to systematically assess convective coupling mechanisms across a broad spectrum of phenomena, this difference in vertical tilt may limit the ability of a vertically integrated quantity such as CSF to provide such a systematic assessment. Second, the degree to which CSF-correlated processes impacting convection contribute to the shape of the empirical CSF–precipitation relationship over tropical oceans remains unclear. The potential influence of CSF-correlated

processes is a point of caution in drawing physical interpretations from the empirical CSF–precipitation relationship, and by extension $r$-diagnosed precipitation.

In this study, we have used CSF, a bulk measure of column-integrated moisture that neglects vertical structure, as a rough proxy for buoyancy. By comparing CSF to convective activity, we have been able to gain insight as to when the behavior of this proxy approximates that of true buoyancy, and when it does not. Several results of this study motivate the use of a more detailed, holistic buoyancy framework, which takes into consideration both temperature and moisture variations, as well as their vertical structure. Such an analysis is the aim of our current work.

## APPENDIX

### Geographical Variability of the CSF–Precipitation Relationship

When comparing individual ocean basins, Bretherton et al. (2004) found relatively little variability in the CSF–precipitation relationship, suggesting the simple relationship may have broad applicability to tropical convection. Yet subsequent studies have noted important departures from this more "generic" tropical oceanic CSF–precipitation relationship. Ahmed and Schumacher (2017) showed that the CSF–precipitation relationship over many tropical land areas is characterized by a much earlier and more gradual pickup than the "generic" tropical oceanic relationship. This pickup was largely driven by daytime heating over land, which allowed deep convection and precipitation to occur even in relatively dry environments. Bergemann and Jakob (2016) similarly documented an early and gradual pickup in the CSF–precipitation relationship of coastal precipitation, where land–sea interactions (e.g., organization along sea-breeze

fronts) allow precipitation to develop in relatively dry environments. Ahmed and Schumacher (2017) also documented more subtle variability in the CSF–precipitation curve over tropical oceans, suggesting that changing thermodynamic conditions may manifest themselves in nuanced variations in the CSF–precipitation curve.

In an effort to establish causality in the CSF–precipitation relationship (i.e., establish if the atmosphere is moist because it is raining or if it is raining because the atmosphere is moist), Kuo et al. (2017) varied entrainment in the Community Earth System Model from 0 through its nominal value of 1 to a doubled value of 2. When entrainment was turned off, precipitation began at very low values of column water vapor (CWV) and increased roughly linearly with increasing CWV (i.e., an early and gradual pickup). In contrast, when entrainment was doubled from its nominal value, precipitation was suppressed until high values of CWV, at which point it increased roughly exponentially with CWV (i.e., a late and steep pickup). These results, taken together with the findings of Bergemann and Jakob (2016) and Ahmed and Schumacher (2017), suggest that the late and steep pickup of the CSF–precipitation curve is the signature of entrainment successfully suppressing convection until high levels of environmental humidity have been achieved. Conversely, the early and gradual pickup of the CSF–precipitation curve is indicative of the absence of the limiting effects of entrainment, either because some other process helps convection overcome the limiting effects of entrainment (e.g., diurnal heating over land or dynamical forcing along a sea-breeze front) or because entrainment itself is weak or missing (e.g., poor model representation).

Figure A1 shows the geographical dependence of the CSF–precipitation relationship, presented in terms of CSF–precipitation curves for select locations (Fig. A1c) and maps of the $a_d$ and $r_d$ parameters (Figs. A1a,b, respectively). CSF–precipitation curves were calculated following the methodology outlined in section 2, using a moving 15° latitude × 45° longitude window, where only oceanic observations were used. Note that the geographical dependence of the CSF–precipitation relationship does not follow climatologically moist and rainy areas (black contour). This indicates that the processes determining the shape of the CSF–precipitation curve vary independently from the processes determining the proclivity of a given geographical location to spend time in the rainy part of the curve (Neelin et al. 2009). The CSF–precipitation curves for the Philippines (red line), central Indian Ocean (orange line), east Pacific ITCZ (yellow line), and central Pacific ITCZ (light blue line), all climatologically rainy regions of the tropics, are very similar at CSFs below 0.75. Above this point the curves begin to diverge more, with the former locations showing a
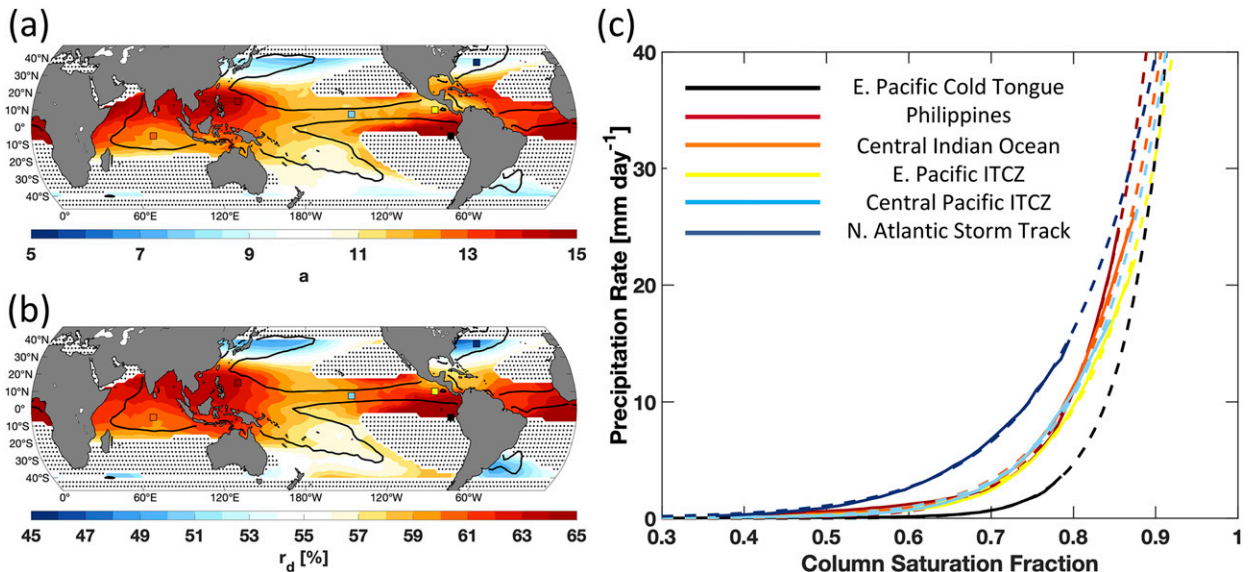
FIG. A1. The geographical dependence of the column saturation fraction (CSF)–precipitation relationship for 6-hourly TRMM precipitation and ERAi CSF, as captured by the (a) $a_d$ and (b) $r_d$ parameters in Eq. (1). Calculations were done using a moving 15° latitude × 45° longitude window, where only oceanic observations were used. Solid black contours are the 4 mm day$^{-1}$ contour of climatological precipitation. Stippling denotes regions of insufficient data for the curve-fitting algorithm. Further details of the curve-fitting algorithm are provided in section 2. (c) Bin-mean precipitation as a function of CSF (solid lines) and the least squares fit of Eq. (1) (dashed lines) for various geographical locations. The colored boxes in (a) and (b) correspond to the colored curves in (c).

more rapid increase in precipitation with CSF than the latter locations. Decreased values of $a_d$ and $r_d$ in the central and eastern Pacific, regions of strong SST driven convergence and more frequent midlatitude intrusions, may be related to the influence of dynamical forcing on the CSF–precipitation relationship (Back and Bretherton 2009a,b). South of the east Pacific ITCZ (black line), where SST begins to cool, precipitation does not begin to increase until a much higher CSF, possibly reflecting reduced surface-based instability. Poleward of ~20° the "late and steep" CSF–precipitation curves of the tropics quickly transition to the "early and gradual" curves of the extratropics (dark blue curve), where precipitation is often associated with strong dynamic forcing by baroclinic systems. The early rise of the CSF–precipitation curve is particularly evident over regions of western boundary currents. Seasonal variability is evident in the geographical dependence of the CSF–precipitation curve (not shown).

While we cannot offer physical explanations for all the variations in the CSF–precipitation relationship (e.g., the maxima near the Philippines), the results of this section correspond well with the results of Ahmed and Schumacher (2017), who used a different methodology to assess geographical dependence of the CSF–precipitation curve, lending confidence to the overall robustness of these relationships. While more universal moisture–precipitation relationships (i.e., exhibiting less geographical dependence)

have been documented (Peters and Neelin 2006; Neelin et al. 2009), the relatively simple functional form of Eq. (1) makes it an appealing relationship for investigating CCEWs.

REFERENCES

Adames, Á. F., 2017: Precipitation budget of the Madden–Julian oscillation. *J. Atmos. Sci.*, **74**, 1799–1817, https://doi.org/10.1175/JAS-D-16-0242.1.

——, and D. Kim, 2016: The MJO as a dispersive, convectively coupled moisture wave: Theory and observations. *J. Atmos. Sci.*, **73**, 913–941, https://doi.org/10.1175/JAS-D-15-0170.1.

——, and Y. Ming, 2018: Interactions between water vapor and potential vorticity in synoptic-scale monsoonal disturbances: Moisture vortex instability. *J. Atmos. Sci.*, **75**, 2083–2106, https://doi.org/10.1175/JAS-D-17-0310.1.

——, D. Kim, S. K. Clark, Y. Ming, and K. Inoue, 2019: Scale analysis of moist thermodynamics in a simple model and the relationship between moisture modes and gravity waves. *J. Atmos. Sci.*, **76**, 3863–3881, https://doi.org/10.1175/JAS-D-19-0121.1.

Ahmed, F., and C. Schumacher, 2015: Convective and stratiform components of the precipitation-moisture relationship. *Geophys. Res. Lett.*, **42**, 10 453–10 462, https://doi.org/10.1002/2015GL066957.

——, and ——, 2017: Geographical differences in the tropical precipitation-moisture relationship and rain intensity onset. *Geophys. Res. Lett.*, **44**, 1114–1122, https://doi.org/10.1002/2016GL071980.

——, and J. D. Neelin, 2018: Reverse engineering the tropical precipitation–buoyancy relationship. *J. Atmos. Sci.*, **75**, 1587–1608, https://doi.org/10.1175/JAS-D-17-0333.1.

Ahn, M.-S., D. Kim, K. R. Sperber, I.-S. Kang, E. Maloney, D. Waliser, and H. Hendon, 2017: MJO simulation in CMIP5 climate models: MJO skill metrics and process-oriented diagnosis. *Climate Dyn.*, **49**, 4023–4045, https://doi.org/10.1007/s00382-017-3558-4.

Andersen, J. A., and Z. Kuang, 2012: Moist static energy budget of MJO-like disturbances in the atmosphere of a zonally symmetric aquaplanet. *J. Climate*, **25**, 2782–2804, https://doi.org/10.1175/JCLI-D-11-00168.1.

Arnold, N. P., M. Branson, Z. Kuang, D. A. Randall, and E. Tziperman, 2015: MJO intensification with warming in the superparameterized CESM. *J. Climate*, **28**, 2706–2724, https://doi.org/10.1175/JCLI-D-14-00494.1.

Avila, L. A., and J. L. Guiney, 2000: Eastern North Pacific hurricane season of 1998. *Mon. Wea. Rev.*, **128**, 2990–3000, https://doi.org/10.1175/1520-0493(2000)128<2990:ENPHSO>2.0.CO;2.

Back, L. E., and C. S. Bretherton, 2009a: On the relationship between SST gradients, boundary layer winds, and convergence over the tropical oceans. *J. Climate*, **22**, 4182–4196, https://doi.org/10.1175/2009JCLI2392.1.

——, and ——, 2009b: A simple model of climatological rainfall and vertical motion patterns over the tropical oceans. *J. Climate*, **22**, 6477–6497, https://doi.org/10.1175/2009JCLI2393.1.

Benedict, J. J., and D. A. Randall, 2009: Structure of the Madden–Julian oscillation in the superparameterized CAM. *J. Atmos. Sci.*, **66**, 3277–3296, https://doi.org/10.1175/2009JAS3030.1.

Bergemann, M., and C. Jakob, 2016: How important is tropospheric humidity for coastal rainfall in the tropics? *Geophys. Res. Lett.*, **43**, 5860–5868, https://doi.org/10.1002/2016GL069255.

Bretherton, C. S., M. E. Peters, and L. E. Back, 2004: Relationships between water vapor path and precipitation over the tropical oceans. *J. Climate*, **17**, 1517–1528, https://doi.org/10.1175/1520-0442(2004)017<1517:RBWVPA>2.0.CO;2.

Cheng, Y.-M., C. D. Thorncroft, and G. N. Kiladis, 2019: Two contrasting African easterly wave behaviors. *J. Atmos. Sci.*, **76**, 1753–1768, https://doi.org/10.1175/JAS-D-18-0300.1.

Dee, D., and Coauthors, 2011: The ERA-Interim reanalysis: Configuration and performance of the data assimilation system. *Quart. J. Roy. Meteor. Soc.*, **137**, 553–597, https://doi.org/10.1002/qj.828.

Dias, J., and G. N. Kiladis, 2016: The relationship between equatorial mixed Rossby–gravity and eastward inertio-gravity waves. Part II. *J. Atmos. Sci.*, **73**, 2147–2163, https://doi.org/10.1175/JAS-D-15-0231.1.

——, M. Gehne, G. N. Kiladis, N. Sakaeda, P. Bechtold, and T. Haiden, 2018: Equatorial waves and the skill of NCEP and ECMWF numerical weather prediction systems. *Mon. Wea. Rev.*, **146**, 1763–1784, https://doi.org/10.1175/MWR-D-17-0362.1.

Dickinson, M., and J. Molinari, 2002: Mixed Rossby–gravity waves and western Pacific tropical cyclogenesis. Part I: Synoptic evolution. *J. Atmos. Sci.*, **59**, 2183–2196, https://doi.org/10.1175/1520-0469(2002)059<2183:MRGWAW>2.0.CO;2.

Fuchs, Ž., S. L. Sessions, and D. J. Raymond, 2014: Mechanisms controlling the onset of simulated convectively coupled Kelvin waves. *Tellus*, **66A**, 22107, https://doi.org/10.3402/tellusa.v66.22107.

Gonzalez, A. O., and X. Jiang, 2019: Distinct propagation characteristics of intraseasonal variability over the tropical west Pacific. *J. Geophys. Res. Atmos.*, **124**, 5332–5351, https://doi.org/10.1029/2018JD029884.

Grabowski, W. W., 2001: Coupling cloud processes with the large-scale dynamics using the Cloud-Resolving Convection Parameterization (CRCP). *J. Atmos. Sci.*, **58**, 978–997, https://doi.org/10.1175/1520-0469(2001)058<0978:CCPWTL>2.0.CO;2.

Hannah, W. M., and E. D. Maloney, 2014: The moist static energy budget in NCAR CAM5 hindcasts during DYNAMO. *J. Adv. Model. Earth Syst.*, **6**, 420–440, https://doi.org/10.1002/2013MS000272.

Herman, M. J., Z. Fuchs, D. J. Raymond, and P. Bechtold, 2016: Convectively coupled Kelvin waves: From linear theory to global models. *J. Atmos. Sci.*, **73**, 407–428, https://doi.org/10.1175/JAS-D-15-0153.1.

Huffman, G. J., and Coauthors, 2007: The TRMM Multisatellite Precipitation Analysis (TMPA): Quasi-global, multiyear, combined-sensor precipitation estimates at fine scales. *J. Hydrometeor.*, **8**, 38–55, https://doi.org/10.1175/JHM560.1.

Hung, M.-P., J.-L. Lin, W. Wang, D. Kim, T. Shinoda, and S. J. Weaver, 2013: MJO and convectively coupled equatorial waves simulated by CMIP5 climate models. *J. Climate*, **26**, 6185–6214, https://doi.org/10.1175/JCLI-D-12-00541.1.

Inoue, K., and L. E. Back, 2017: Gross moist stability analysis: Assessment of satellite-based products in the GMS plane. *J. Atmos. Sci.*, **74**, 1819–1837, https://doi.org/10.1175/JAS-D-16-0218.1.

Khouider, B., and A. J. Majda, 2006: A simple multicloud parameterization for convectively coupled tropical waves. Part I: Linear analysis. *J. Atmos. Sci.*, **63**, 1308–1323, https://doi.org/10.1175/JAS3677.1.

——, and ——, 2008: Multicloud models for organized tropical convection: Enhanced congestus heating. *J. Atmos. Sci.*, **65**, 895–914, https://doi.org/10.1175/2007JAS2408.1.

Kiladis, G. N., C. D. Thorncroft, and N. M. Hall, 2006: Three-dimensional structure and dynamics of African easterly waves. Part I: Observations. *J. Atmos. Sci.*, **63**, 2212–2230, https://doi.org/10.1175/JAS3741.1.

——, M. C. Wheeler, P. T. Haertel, K. H. Straub, and P. E. Roundy, 2009: Convectively coupled equatorial waves. *Rev. Geophys.*, **47**, RG2003, https://doi.org/10.1029/2008RG000266.

——, J. Dias, K. H. Straub, M. C. Wheeler, S. N. Tulich, K. Kikuchi, K. M. Weickmann, and M. J. Ventrice, 2014: A comparison of OLR and circulation-based indices for tracking the MJO. *Mon. Wea. Rev.*, **142**, 1697–1715, https://doi.org/10.1175/MWR-D-13-00301.1.

——, ——, and M. Gehne, 2016: The relationship between equatorial mixed Rossby–gravity and eastward inertio-gravity waves. Part I. *J. Atmos. Sci.*, **73**, 2123–2145, https://doi.org/10.1175/JAS-D-15-0230.1.

Kuang, Z., 2008: A moisture-stratiform instability for convectively coupled waves. *J. Atmos. Sci.*, **65**, 834–854, https://doi.org/10.1175/2007JAS2444.1.

Kuo, Y.-H., J. D. Neelin, and C. R. Mechoso, 2017: Tropical convective transition statistics and causality in the water vapor–precipitation relation. *J. Atmos. Sci.*, **74**, 915–931, https://doi.org/10.1175/JAS-D-16-0182.1.

Lau, K.-H., and N.-C. Lau, 1992: The energetics and propagation dynamics of tropical summertime synoptic-scale disturbances. *Mon. Wea. Rev.*, **120**, 2523–2539, https://doi.org/10.1175/1520-0493(1992)120<2523:TEAPDO>2.0.CO;2.

Lau, W. K., and D. E. Waliser, 2012: *Intraseasonal Variability in the Atmosphere-Ocean Climate System.* Springer, 614 pp.

Majda, A. J., and S. N. Stechmann, 2009: The skeleton of tropical intraseasonal oscillations. *Proc. Natl. Acad. Sci. USA*, **106**, 8417–8422, https://doi.org/10.1073/pnas.0903367106.

Mapes, B. E., 2000: Convective inhibition, subgrid-scale triggering energy, and stratiform instability in a toy tropical wave model. *J. Atmos. Sci.*, **57**, 1515–1535, https://doi.org/10.1175/1520-0469(2000)057<1515:CISSTE>2.0.CO;2.

Matsuno, T., 1966: Quasi-geostrophic motions in the equatorial area. *J. Meteor. Soc. Japan*, **44**, 25–43, https://doi.org/10.2151/jmsj1965.44.1_25.

Matthews, A. J., B. J. Hoskins, and M. Masutani, 2004: The global response to tropical heating in the Madden–Julian oscillation during the northern winter. *Quart. J. Roy. Meteor. Soc.*, **130**, 1991–2011, https://doi.org/10.1256/qj.02.123.

Moncrieff, M. W., C. Liu, and P. Bogenschutz, 2017: Simulation, modeling, and dynamically based parameterization of organized tropical convection for global climate models. *J. Atmos. Sci.*, **74**, 1363–1380, https://doi.org/10.1175/JAS-D-16-0166.1.

Neelin, J. D., and I. M. Held, 1987: Modeling tropical convergence based on the moist static energy budget. *Mon. Wea. Rev.*, **115**, 3–12, https://doi.org/10.1175/1520-0493(1987)115<0003: MTCBOT>2.0.CO;2.

——, O. Peters, and K. Hales, 2009: The transition to strong convection. *J. Atmos. Sci.*, **66**, 2367–2384, https://doi.org/10.1175/2009JAS2962.1.

North, G. R., T. L. Bell, R. F. Cahalan, and F. J. Moeng, 1982: Sampling errors in the estimation of empirical orthogonal functions. *Mon. Wea. Rev.*, **110**, 699–706, https://doi.org/10.1175/1520-0493(1982)110<0699:SEITEO>2.0.CO;2.

Peters, O., and J. D. Neelin, 2006: Critical phenomena in atmospheric precipitation. *Nat. Phys.*, **2**, 393–396, https://doi.org/10.1038/nphys314.

Powell, S. W., 2017: Successive MJO propagation in MERRA-2 reanalysis. *Geophys. Res. Lett.*, **44**, 5178–5186, https://doi.org/10.1002/2017GL073399.

——, and R. A. Houze Jr., 2015: Effect of dry large-scale vertical motions on initial MJO convective onset. *J. Geophys. Res. Atmos.*, **120**, 4783–4805, https://doi.org/10.1002/2014JD022961.

Pritchard, M. S., and C. S. Bretherton, 2014: Causal evidence that rotational moisture advection is critical to the superparameterized Madden–Julian oscillation. *J. Atmos. Sci.*, **71**, 800–815, https://doi.org/10.1175/JAS-D-13-0119.1.

Randall, D., M. Khairoutdinov, A. Arakawa, and W. Grabowski, 2003: Breaking the cloud parameterization deadlock. *Bull. Amer. Meteor. Soc.*, **84**, 1547–1564, https://doi.org/10.1175/BAMS-84-11-1547.

Raymond, D. J., 2001: A new model of the Madden–Julian oscillation. *J. Atmos. Sci.*, **58**, 2807–2819, https://doi.org/10.1175/1520-0469(2001)058<2807:ANMOTM>2.0.CO;2.

——, and Ž. Fuchs, 2007: Convectively coupled gravity and moisture modes in a simple atmospheric model. *Tellus*, **59A**, 627–640, https://doi.org/10.1111/j.1600-0870.2007.00268.x.

——, and ——, 2009: Moisture modes and the Madden–Julian oscillation. *J. Climate*, **22**, 3031–3046, https://doi.org/10.1175/2008JCLI2739.1.

——, S. L. Sessions, A. H. Sobel, and Ž. Fuchs, 2009: The mechanics of gross moist stability. *J. Adv. Model. Earth Syst.*, **1** (3), https://doi.org/10.3894/JAMES.2009.1.9.

Roundy, P. E., 2012a: Observed structure of convectively coupled waves as a function of equivalent depth: Kelvin waves and the Madden–Julian oscillation. *J. Atmos. Sci.*, **69**, 2097–2106, https://doi.org/10.1175/JAS-D-12-03.1.

——, 2012b: The spectrum of convectively coupled Kelvin waves and the Madden–Julian oscillation in regions of low-level easterly and westerly background flow. *J. Atmos. Sci.*, **69**, 2107–2111, https://doi.org/10.1175/JAS-D-12-060.1.

Rushley, S., D. Kim, C. Bretherton, and M.-S. Ahn, 2018: Reexamining the nonlinear moisture-precipitation relationship over the tropical oceans. *Geophys. Res. Lett.*, **45**, 1133–1140, https://doi.org/10.1002/2017GL076296.

Rydbeck, A. V., and E. D. Maloney, 2014: Energetics of east Pacific easterly waves during intraseasonal events. *J. Climate*, **27**, 7603–7621, https://doi.org/10.1175/JCLI-D-14-00211.1.

——, and ——, 2015: On the convective coupling and moisture organization of east Pacific easterly waves. *J. Atmos. Sci.*, **72**, 3850–3870, https://doi.org/10.1175/JAS-D-15-0056.1.

Serra, Y. L., G. N. Kiladis, and M. F. Cronin, 2008: Horizontal and vertical structure of easterly waves in the Pacific ITCZ. *J. Atmos. Sci.*, **65**, 1266–1284, https://doi.org/10.1175/2007JAS2341.1.

Sobel, A. H., and D. Kim, 2012: The MJO-Kelvin wave transition. *Geophys. Res. Lett.*, **39**, L20808, https://doi.org/10.1029/2012GL053380.

——, J. Nilsson, and L. M. Polvani, 2001: The weak temperature gradient approximation and balanced tropical moisture waves. *J. Atmos. Sci.*, **58**, 3650–3665, https://doi.org/10.1175/1520-0469(2001)058<3650:TWTGAA>2.0.CO;2.

Straub, K. H., and G. N. Kiladis, 2003: The observed structure of convectively coupled Kelvin waves: Comparison with simple models of coupled wave instability. *J. Atmos. Sci.*, **60**, 1655–1668, https://doi.org/10.1175/1520-0469(2003)060<1655:TOSOCC>2.0.CO;2.

Thorncroft, C., and B. Hoskins, 1994a: An idealized study of African easterly waves. I: A linear view. *Quart. J. Roy. Meteor. Soc.*, **120**, 953–982, https://doi.org/10.1002/qj.49712051809.

——, and ——, 1994b: An idealized study of African easterly waves. II: A nonlinear view. *Quart. J. Roy. Meteor. Soc.*, **120**, 983–1015, https://doi.org/10.1002/qj.49712051810.

——, and K. Hodges, 2001: African easterly wave variability and its relationship to Atlantic tropical cyclone activity. *J. Climate*, **14**, 1166–1179, https://doi.org/10.1175/1520-0442(2001)014<1166:AEWVAI>2.0.CO;2.

Tulich, S. N., and B. E. Mapes, 2010: Transient environmental sensitivities of explicitly simulated tropical convection. *J. Atmos. Sci.*, **67**, 923–940, https://doi.org/10.1175/2009JAS3277.1.

Wang, B., F. Liu, and G. Chen, 2016: A trio-interaction theory for Madden–Julian oscillation. *Geosci. Lett.*, **3**, 34, https://doi.org/10.1186/s40562-016-0066-z.

Wheeler, M., and G. N. Kiladis, 1999: Convectively coupled equatorial waves: Analysis of clouds and temperature in the wavenumber–frequency domain. *J. Atmos. Sci.*, **56**, 374–399, https://doi.org/10.1175/1520-0469(1999)056<0374:CCEWAO>2.0.CO;2.

Wolding, B. O., and E. D. Maloney, 2015: Objective diagnostics and the Madden–Julian oscillation. Part II: Application to moist static energy and moisture budgets. *J. Climate*, **28**, 7786–7808, https://doi.org/10.1175/JCLI-D-14-00689.1.

——, ——, and M. Branson, 2016: Vertically resolved weak temperature gradient analysis of the Madden-Julian oscillation in SP-CESM. *J. Adv. Model. Earth Syst.*, **8**, 1586–1619, https://doi.org/10.1002/2016MS000724.

——, ——, S. Henderson, and M. Branson, 2017: Climate change and the Madden-Julian oscillation: A vertically resolved weak temperature gradient analysis. *J. Adv. Model. Earth Syst.*, **9**, 307–331, https://doi.org/10.1002/2016MS000843.

——, J. Dias, G. Kiladis, F. Ahmed, S. W. Powell, E. Maloney, and M. Branson, 2020: Interactions between moisture and tropical convection. Part I: The coevolution of moisture and convection. *J. Atmos. Sci.*, **77**, 1783–1799, https://doi.org/10.1175/JAS-D-19-0225.1.

Yasunaga, K., and B. Mapes, 2012: Differences between more divergent and more rotational types of convectively coupled equatorial waves. Part I: Space–time spectral analyses. *J. Atmos. Sci.*, **69**, 3–16, https://doi.org/10.1175/JAS-D-11-033.1.

——, S. Yokoi, K. Inoue, and B. E. Mapes, 2019: Space–time spectral analysis of the moist static energy budget equation. *J. Climate*, **32**, 501–529, https://doi.org/10.1175/JCLI-D-18-0334.1.

Zhang, C., 2005: Madden-Julian oscillation. *Rev. Geophys.*, **43**, RG2003, https://doi.org/10.1029/2004RG000158.